catalysts

MDPI

Article

Visible Light Photocatalytic Activity of $NaYF_4$:(Yb,Er)-CuO/TiO_2 Composite

Shielah Mavengere [1], Sang-Chul Jung [2] and Jung-Sik Kim [1,*]

1 Department of Materials Science and Engineering, University of Seoul, Seoul 02504, Korea; lashiema@gmail.com
2 Department of Environmental Engineering, Sunchon National University, Jeonnam 57922, Korea; jsc@sunchon.ac.kr
* Correspondence: jskim@uos.ac.kr; Tel.: +82-2-6490-2409

Received: 10 October 2018; Accepted: 31 October 2018; Published: 5 November 2018

Abstract: TiO_2 photocatalysts are limited to ultraviolet light photo-activation, however, by coupling with $NaYF_4$:(Yb,Er) they can utilize visible light activation, but with low efficiencies. In order to enhance visible light photo-activity, CuO nanoparticles were coupled with $NaYF_4$:(Yb,Er) by mechanical ball-milling and coated with TiO_2-sol. The coupling of CuO nanoparticles with $NaYF_4$:(Yb,Er)/TiO_2 caused the formation of a $NaYF_4$:(Yb,Er)-CuO/TiO_2 composite capable of visible absorption with a remarkably reduced band gap of ~2.5 eV. The $NaYF_4$:(Yb,Er)-CuO/TiO_2 composite in H_2O_2 showed the most efficient methylene blue (MB) degradation efficiency of more than 99.5% after exposure to visible light.

Keywords: $NaYF_4$:(Yb,Er)-CuO/TiO_2; composites; visible light; photocatalyst

1. Introduction

TiO_2, as a semiconductor, is well known for its chemical stability, non-toxicity and ultraviolet (UV) photo-activation [1,2]. This UV photo-activation limits TiO_2 to partial utilization of the solar spectrum (3–5%) [3]. Several research studies have been conducted to reduce the TiO_2 band gap and render it photo-active in the visible region [4,5]. These methods include doping with metal ions (Ag, Co, Fe, Cr, etc.) [6–8], non-metals (N, C, F, etc.) [9,10] and coupling TiO_2 with metal oxides (SiO_2, SnO_2, WO_3, etc.) [11–13] or phosphor materials ($CaAl_2O_4$:(Eu,Nd), $NaYF_4$:(Yb,Er)) [14–16].

Interestingly, the coupling of TiO_2 with upconversion phosphors can remarkably extend utilization of the whole solar spectrum [17]. The major advantage of upconversion phosphor is the ability to convert even low near-infrared (NIR) photons to higher energy photons in the UV and visible light range [18,19]. In this way, the $NaYF_4$:(Yb, Er) upconversion phosphor characteristic emerges from Yb^{3+} ions which absorb the 980 nm wavelength spectrum and transfer energy to Er^{3+} ions which then emit visible light photons. Er^{3+} ions emit visible light at 450, 525, and 650 nm wavelengths due to transitions from its ground state $^4I_{15/2}$ to $^4F_{7/2}$, $^4H_{11/2}$, $^4F_{9/2}$ and $^4G_{9/2}$, respectively [20–22]. For this reason, Yb^{3+} ions are termed sensitizers while Er^{3+} ions are activators. The outstanding photo-stability of upconversion phosphors has propelled their extensive research for dye sensitized solar cells, bio-imaging and UV-vis-NIR photocatalysis applications [19,23].

In a $NaYF_4$:(Yb,Er)/TiO_2 composite, $NaYF_4$:(Yb,Er) phosphor can offer an efficient catalyst support and provide the interfacial energy band bending so that the TiO_2 absorption edge can be extended to the visible region [14,22]. However, the visible light photocatalysis of a $NaYF_4$:(Yb,Er)/TiO_2 composite shows low efficiency. For example, complete photo-degradation of dye pollutants mixed with phosphor-TiO_2 photocatalyst occurs after 10 h of exposure to a visible light source [17,24].

Photocatalysis efficiency depends on various factors which include intensity of illuminating light, temperature, concentration of dye pollutants and the amount of doping elements in the photocatalyst

or the amount of photocatalyst in the reactor [25–27]. For instance, high photocatalyst loading in the reactor can significantly improve photocatalysis efficiency [28,29]. This is mainly because more photocatalyst particles increase the number of photo-active sites which enhance the reaction rate [30]. However, upconversion phosphors are synthesized with rare and scarce earth elements which are less cost competitive [31]. Hence, there is a need to synthesize a composite photocatalyst with high photocatalytic ability even at low catalyst loading in the photo-reactor.

One promising method to improve photocatalytic efficiencies involves the synthesis of multi-composites [10,32]. Recently, several upconversion phosphors of multi-composites were synthesized to produce core–shell structures with TiO_2 and a third compound. For example, $NaYF_4$:(Yb,Er)/TiO_2 coupled with SiO_2 has been reported. SiO_2 in the $NaYF_4$:(Yb,Er)/TiO_2 composite can improve photovoltaic efficiency as well as facilitating energy transfer from phosphor to the TiO_2 conduction band [33,34]. However, in this multi-composite, the photocatalytic efficiency is dependent on the thickness of the outer shell. Thus, a thick silica coating can hinder light absorption in the inner phosphor particles. The most important property of a photocatalyst is the ability to maintain chemical stability after a photo-degradation cycle. This photo-stability property is beneficial for recyclability [35,36]. Unfortunately, the core–shell structures are reported to be unstable during separation and centrifuge washing steps. Therefore, recyclability is limited for the core–shell photocatalyst [19].

Surprisingly, the coupling of $NaYF_4$:(Yb,Er)/TiO_2 with visible light-active CuO (1.2–2.0 eV) has not been extensively studied yet. Moreover, CuO is abundantly available, chemically stable and photo-active in H_2O_2 aqueous media [37]. It is important to note that H_2O_2 has been used to remove organic impurities with photocatalytic materials under light exposure [38–40]. The substantial advantage of coupling $NaYF_4$:(Yb,Er) with TiO_2 and CuO is to form composites with improved band structure for efficiently utilizing the broad solar spectrum in photocatalysis [22,33].

In this study, CuO nanoparticles were combined with the $NaYF_4$:(Yb,Er)/TiO_2 composite to enhance visible light absorption and photocatalytic activity. The effect of H_2O_2 on photocatalytic performance and the recyclability of $NaYF_4$:(Yb,Er)-CuO/TiO_2 photocatalyst were also examined.

2. Results and Discussion

Figure 1 shows x-ray diffraction (XRD) patterns for $NaYF_4$:(Yb,Er), CuO, $NaYF_4$:(Yb,Er)-CuO and $NaYF_4$:(Yb,Er)-CuO/TiO_2 composite. The pure phosphor was referenced to the characteristic peaks of JCPDS No. 77-2042 while the CuO nanoparticles were referenced to JCPDS No. 045-0937. With increasing annealing temperature from 350 °C to 550 °C (from Figure 1c–f), the $NaYF_4$:(Yb,Er) phosphor main peaks occurred at (111), (200), (220) and (311) were diminishing. While CuO characteristic peaks corresponding to (002), (111), (202) and (020) emerged along the $NaYF_4$:(Yb,Er)-CuO composites. Besides $NaYF_4$:(Yb,Er) and CuO characteristic peaks, new peaks occurred at 17°, 29°, 30°, 39°, 43°, 53° and 77° and are suggested to be (hexagonal) β-$NaYF_4$. These diffraction peaks corresponding to β-$NaYF_4$ are indexed in JCPDS No. 28-1192 as (100), (110), (101), (111), (201), (300) and (302) respectively. The thermal treatment may have induced the phase transition from α to β-$NaYF_4$. Furthermore, due to the co-existence of three phases (cubic $NaYF_4$, hexagonal $NaYF_4$ and CuO), it is expected that intermetallic compounds are formed during thermal treatment. Although no other Cu phases were identified at different annealing conditions, a 450 °C annealing temperature is known for pure CuO phases with band gaps between 1.2 eV and 2 eV [41]. Therefore, $NaYF_4$:(Yb,Er)-CuO composites annealed at 450 °C were utilized for TiO_2 coating. TiO_2 peaks could not be observed in the $NaYF_4$:(Yb,Er)-CuO/TiO_2 composite because its amount was beyond the XRD detection limit.

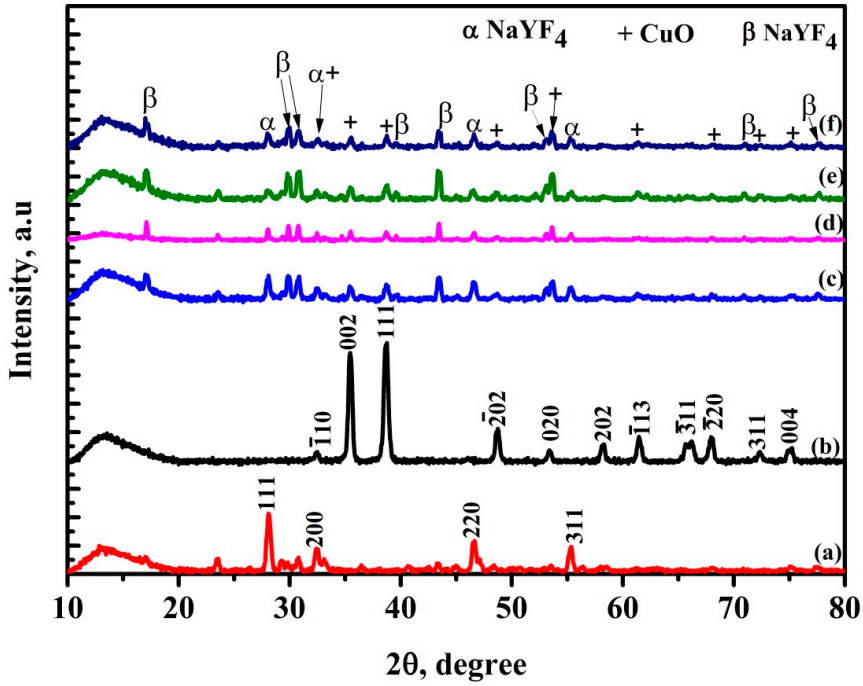

Figure 1. XRD spectra of (**a**) $NaYF_4$:(Yb,Er), (**b**) CuO, (**c**) $NaYF_4$:(Yb,Er)-CuO at 350 °C, (**d**) $NaYF_4$:(Yb,Er)-CuO at 450 °C, (**e**) $NaYF_4$:(Yb,Er)-CuO at 550 °C, and (**f**) $NaYF_4$:(Yb,Er)-CuO/TiO_2 composite at 450 °C.

Figure 2 shows SEM images of (a) $NaYF_4$:(Yb,Er), (b) CuO, (c) $NaYF_4$:(Yb,Er)-CuO, (d) $NaYF_4$:(Yb,Er)-CuO/TiO_2. The prepared $NaYF_4$:(Yb,Er) phosphor has agglomerated particles as shown in Figure 2a around 2 μm in diameter. However, the CuO particles in Figure 2b are dense spherical particles. In Figure 2c, $NaYF_4$:(Yb,Er)-CuO composite powders consist of particles of sizes below 1 μm. It is evident that mechanical ball-milling might reduce the size of $NaYF_4$:(Yb,Er) phosphor agglomerates. The $NaYF_4$:(Yb,Er)-CuO/TiO_2 composite in Figure 2d consists of agglomerates with dense particles of nanometer range, due to TiO_2 coating. Figure 2e shows the particle size distribution for the $NaYF_4$:(Yb,Er)-CuO/TiO_2 composite. The particle sizes are ranging between 0.8 and 4 μm. The EDS spectra for the $NaYF_4$:(Yb,Er)-CuO/TiO_2 composite confirmed the presence of all elements, as shown in Figure 2f.

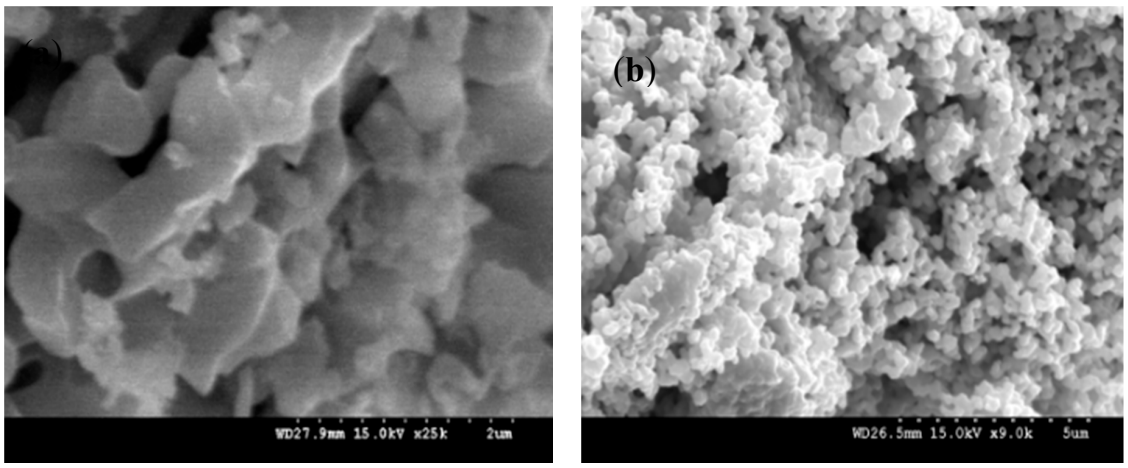

Figure 2. *Cont.*

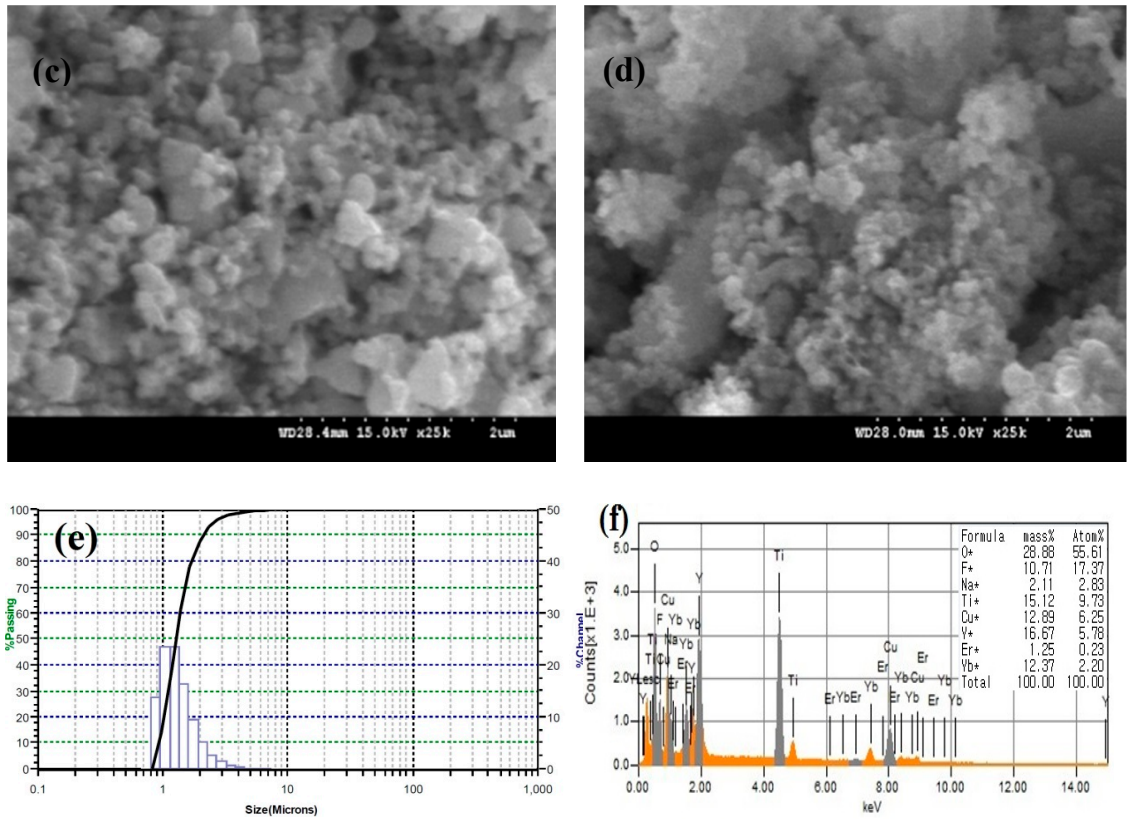

Figure 2. SEM images of (**a**) $NaYF_4$:(Yb,Er), ×25k, (**b**) CuO, ×9k, (**c**) $NaYF_4$:(Yb,Er)-CuO, ×25k, (**d**) $NaYF_4$:(Yb,Er)-CuO/TiO_2, x25k, (**e**) particle size distribution of $NaYF_4$:(Yb,Er)-CuO/TiO_2 composite and (**f**) EDS spectra for the $NaYF_4$:(Yb,Er)-CuO/TiO_2 composite.

Figure 3 shows N_2 adsorption-desorption isotherms for the $NaYF_4$:(Yb,Er)/TiO_2 and $NaYF_4$:(Yb,Er)-CuO/TiO_2 photocatalyst composites. The specific surface areas in the table insert in Figure 3 are 15.9 m^2/g and 12.4 m^2/g for $NaYF_4$:(Yb,Er)/TiO_2 and $NaYF_4$:(Yb,Er)-CuO/TiO_2, respectively, while the pore size and adsorbed volume are 8.93 nm and 0.0355 cm^3/g for $NaYF_4$:(Yb,Er)/TiO_2 and 13.3 nm and 0.0413 cm^3/g for $NaYF_4$:(Yb,Er)-CuO/TiO_2, respectively. The specific surface area of pure $NaYF_4$:(Yb,Er) in other previous research is 11.5 m^2/g [22]. The differences in the specific surface area, pore volume and diameter are dependent on the synthesis variables and changes in crystalline composition of the photocatalysts. Therefore, the low surface area and high volume adsorbed/pore diameter observed in the $NaYF_4$:(Yb,Er)-CuO/TiO_2 composite confirms the change in crystallinity with CuO nanoparticles coupling.

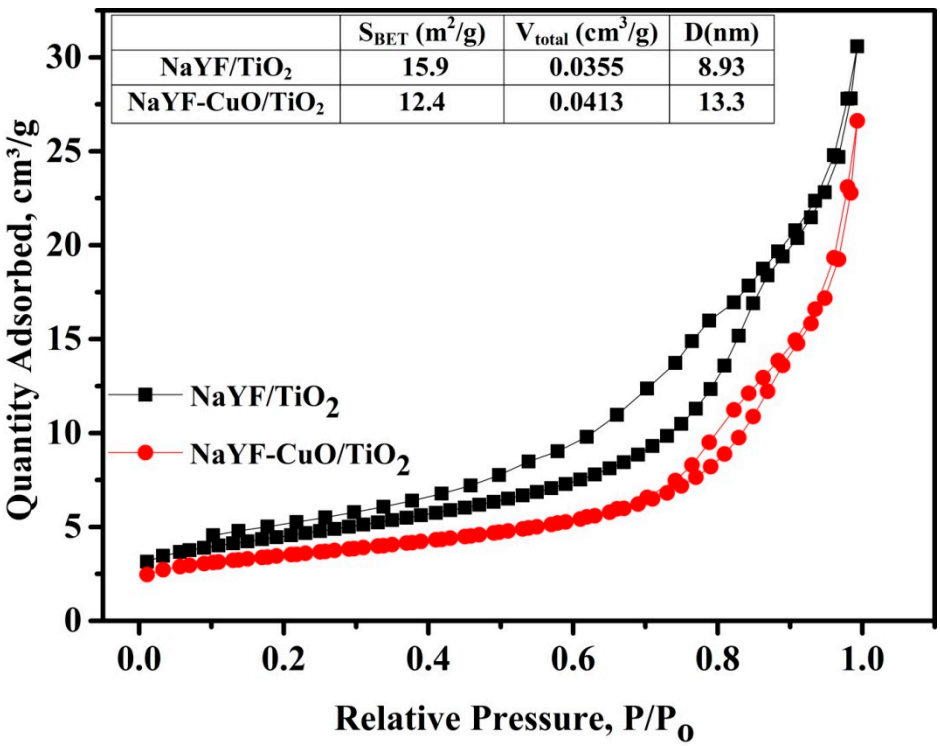

Figure 3. N_2 adsorption-desorption isotherms of $NaYF_4$:(Yb,Er)/TiO_2 and $NaYF_4$:(Yb,Er)-CuO/TiO_2. NaYF represents $NaYF_4$:(Yb,Er).

Figure 4a shows the UV-vis absorption spectra for $NaYF_4$:(Yb,Er), CuO and $NaYF_4$:(Yb,Er)-CuO/TiO_2 samples vs. wavelength. The $NaYF_4$:(Yb,Er)-CuO/TiO_2 composite exhibited similar absorption characteristics to CuO, but with an extended UV absorption edge at 380 nm. This absorption edge is related to both TiO_2 nanoparticles and $NaYF_4$:(Yb,Er). The enlarged UV-vis absorption spectra in Figure 4b clearly shows absorption peaks at 380 nm, 522 nm and 655 nm which are characteristic absorption peaks for $NaYF_4$:(Yb,Er) upconversion phosphors. These Er^{3+} absorption peaks were originated from the ground states $^4I_{15/2}$ to $^4G_{9/2}$, $^4F_{7/2}$ and $^4S_{3/2}$, respectively [42]. However, in the TiO_2 coated $NaYF_4$:(Yb,Er) phosphor, the 380 nm peak is not observed because it corresponds to the TiO_2 absorption range. The estimated band energies for CuO, $NaYF_4$:(Yb,Er)/TiO_2 and $NaYF_4$:(Yb,Er)-CuO/TiO_2 are 1.5 eV, 3.18 eV and 2.5 eV, respectively, as shown in Figure 4c. The remarkable band gap reduction in $NaYF_4$:(Yb,Er)-CuO/TiO_2 typically signifies the composites can be photo-activated with both UV and visible light for photocatalysis reactions.

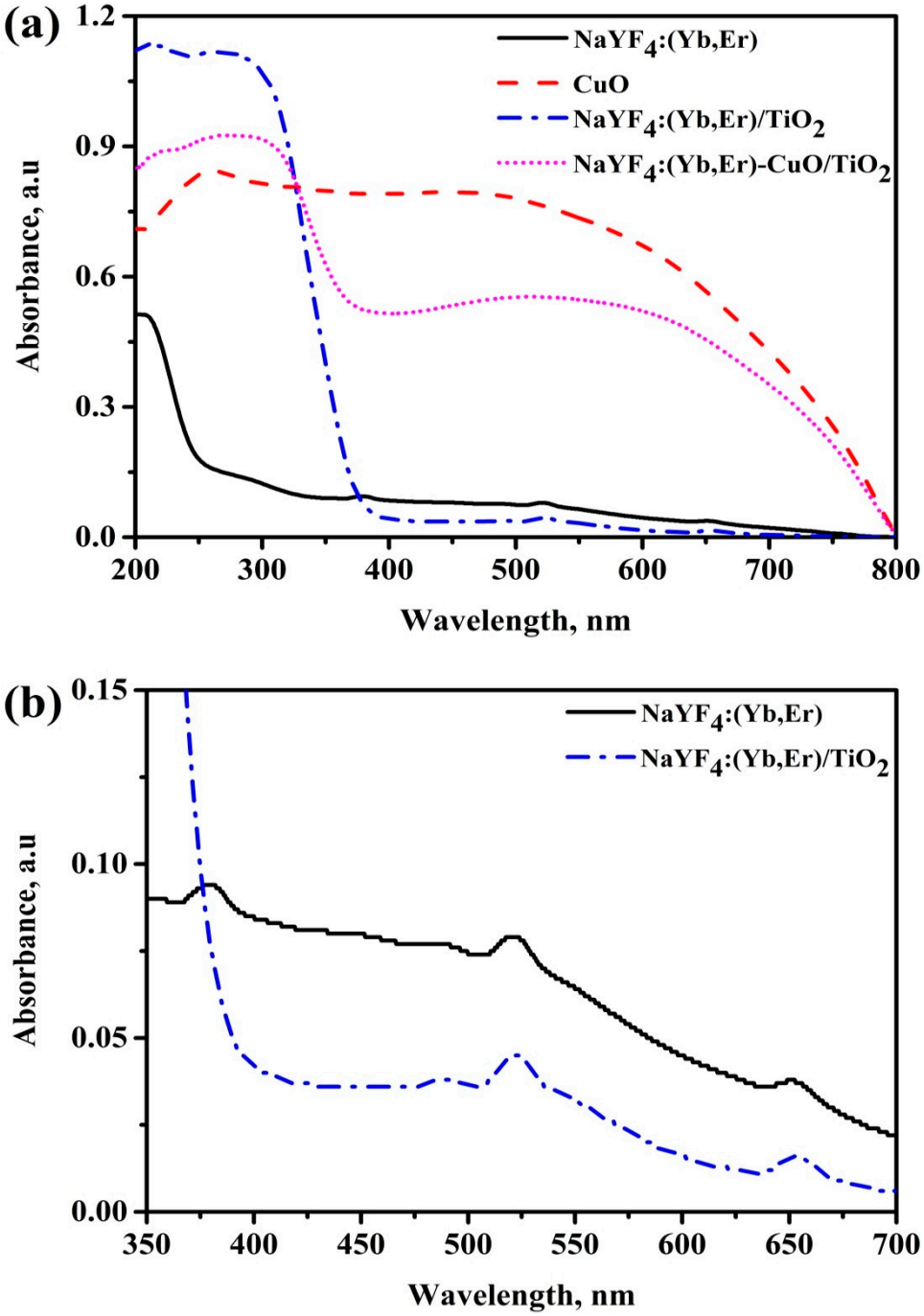

Figure 4. *Cont.*

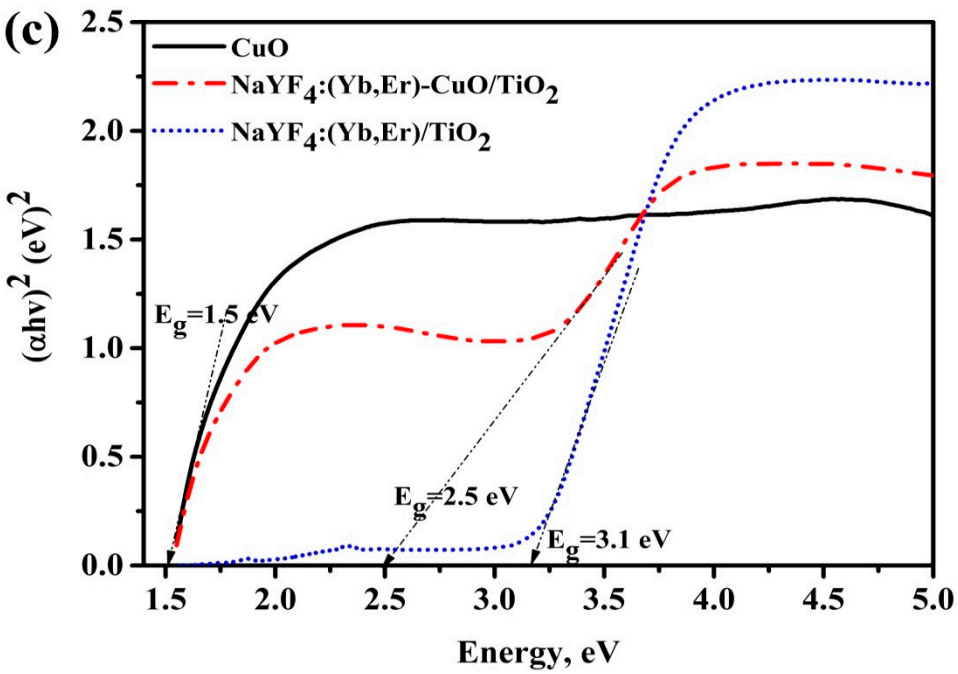

Figure 4. UV-vis diffuse reflectance spectra for (**a**) $NaYF_4$:(Yb,Er), CuO and $NaYF_4$:(Yb,Er)-CuO/TiO_2 composite; (**b**) enlargement spectra at 350–700 nm wavelength axis in (**a**) and (**c**) Kubelka-Munk plots with the band gap energies.

Figure 5a shows the photoluminescence spectra of $NaYF_4$:(Yb,Er), $NaYF_4$:(Yb,Er)-CuO and $NaYF_4$:(Yb,Er)-CuO/TiO_2. The intensity of the photoluminescence (PL) peaks denotes the extent of energy transfer efficiency [18]. Pure $NaYF_4$:(Yb,Er) phosphor has visible light emission peaks at 450 nm, 545 nm, 660 nm and a near infrared peak at 825 nm. However, the emission peaks diminish with coupling $NaYF_4$:(Yb,Er) with CuO nanoparticles, TiO_2 coating on $NaYF_4$:(Yb,Er) phosphor and in $NaYF_4$:(Yb,Er)-CuO composite. Although energy transfer efficiency is evaluated by the decrease in peak intensities, in TiO_2 coated samples, the peak reduction is generally referenced to light emission hindrance by TiO_2 nanoparticles [14]. However, the overall peak suppression can be explained by considering the band structure of the $NaYF_4$:(Yb,Er)-CuO/TiO_2 composite. Figure 5c shows the schematic band structure of the $NaYF_4$:(Yb,Er)-CuO/TiO_2 composite and the energy transfer processes labelled (A), (B), (C) and (D). Firstly, if process (A) is considered as excitation of $NaYF_4$:(Yb,Er) phosphor with 980 nm illumination, because of its luminescent characteristics, energy photons in the visible and NIR are emitted. Thus, as seen in Figure 5a, emission peaks were observed at 450 nm, 545 nm, 660 nm and 825 nm. Secondly, if process (B) is considered as the energy transfer route for light photons emitted from $NaYF_4$:(Yb,Er), the visible light peaks are absorbed by CuO. However, the emission peaks are suppressed at (C) in the $NaYF_4$:(Yb,Er)-CuO composite. Finally, when considering light photons emitted by $NaYF_4$:(Yb,Er) phosphor at (B) are transferred to TiO_2 at (C) via CuO, energy losses are inevitable at (D). The reasons for peak suppression being that energy is lost through multi-phonon vibrations and the blockage of phosphor emission centers by TiO_2 and CuO nanoparticles [17].

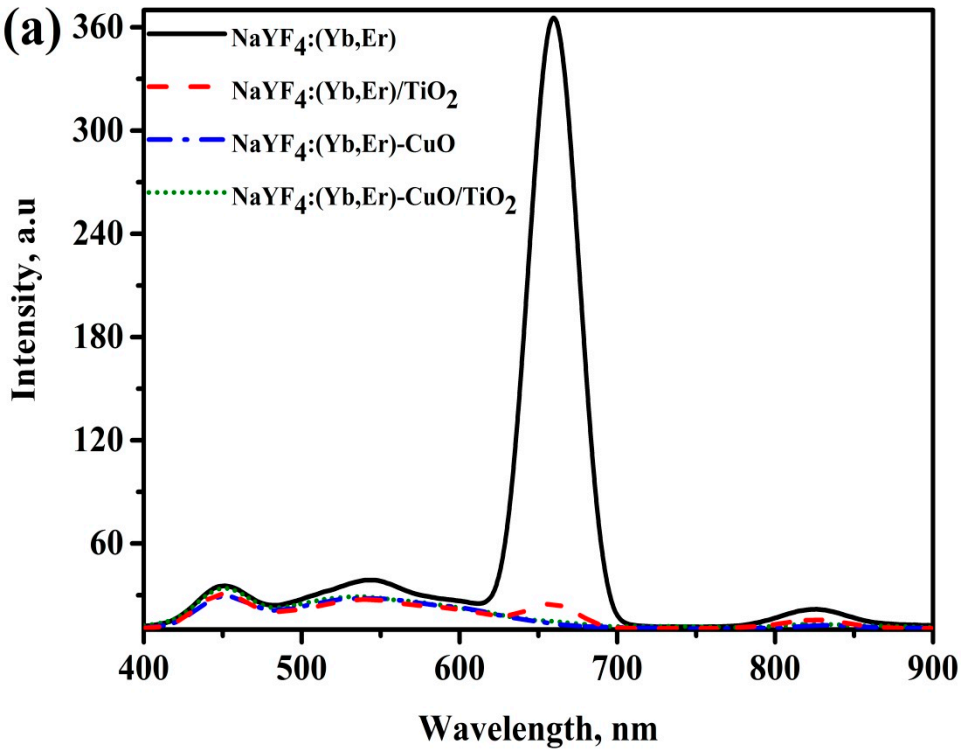

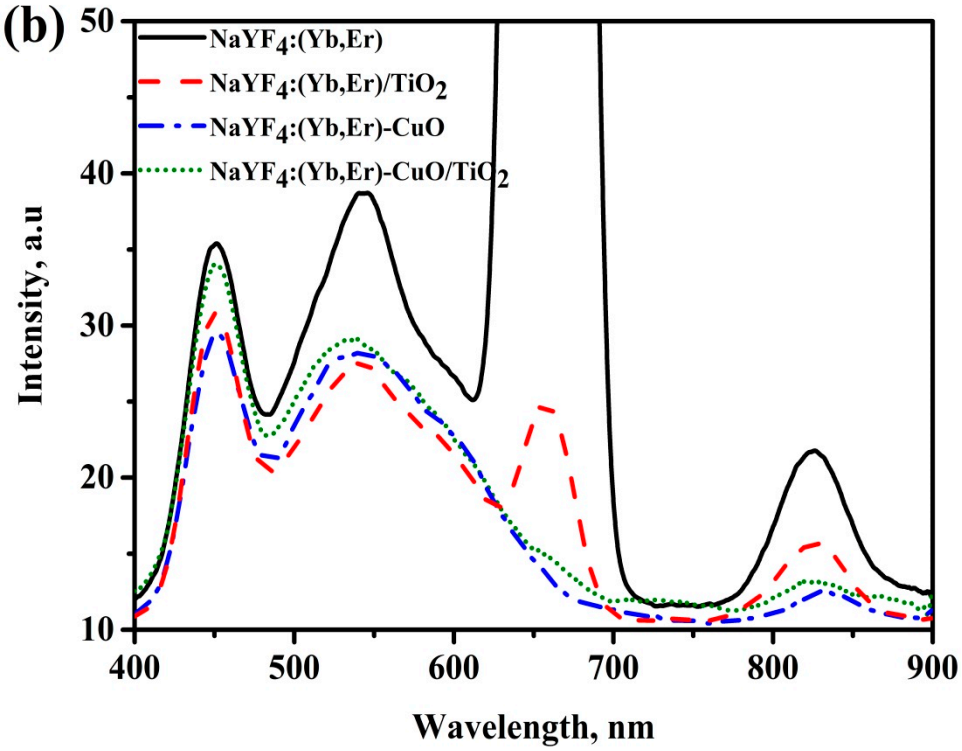

Figure 5. *Cont.*

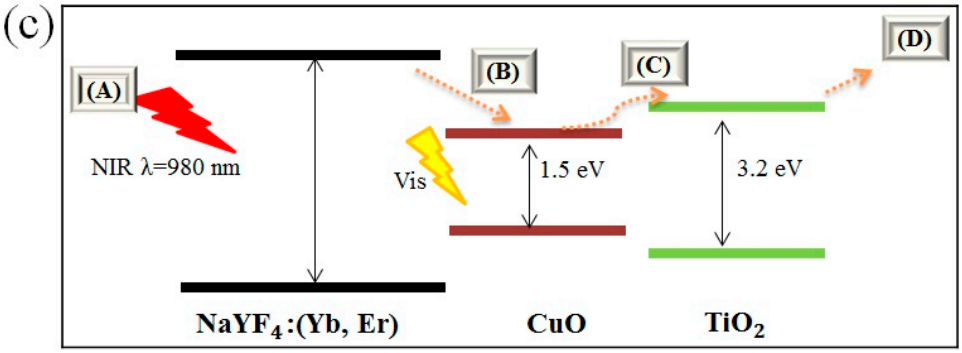

Figure 5. Photoluminescence spectra of (**a**) $NaYF_4$:(Yb,Er), $NaYF_4$:(Yb,Er)-CuO and $NaYF_4$:(Yb,Er)-CuO/TiO_2; (**b**) enlargement spectra at 10 to 50 intensity axes and (**c**) schematic band structure and energy transfer routes in the $NaYF_4$:(Yb,Er)-CuO/TiO_2 composites.

Figure 6a shows the degradation efficiency of the methylene blue (MB) solution with H_2O_2 only (no photocatalyst), without and with H_2O_2 for $NaYF_4$:(Yb,Er)/TiO_2 and $NaYF_4$:(Yb,Er)-CuO/TiO_2 under visible light for 1 h. The $NaYF_4$:(Yb,Er)-CuO/TiO_2 composites exhibit the fastest degradation efficiency, whereby 60% of the MB solution is degraded within 1 h. The photocatalytic reaction of $NaYF_4$:(Yb,Er)/TiO_2 without H_2O_2 oxidant molecules is very slow, but with hydrogen peroxide the reaction is enhanced. This is attributed to the unique role of hydrogen peroxide decomposing in the presence of a photocatalyst and light to give hydroxyl and superoxide ions which attack and degrade MB-dye molecules [39]. The photocatalytic degradation of MB solution with $NaYF_4$:(Yb,Er)-CuO/TiO_2 follows first order reaction kinetics as shown in Figure 6b. The rate constant for $NaYF_4$:(Yb,Er)-CuO/TiO_2 is 0.008 min^{-1}. Whilst for $NaYF_4$:(Yb,Er)/TiO_2 without and with H_2O_2 is 0.0015 min^{-1} and 0.0043 min^{-1}, respectively. Accordingly from the rate constants, the degradation with $NaYF_4$:(Yb,Er)-CuO/TiO_2 is five times and almost two times faster than in $NaYF_4$:(Yb,Er)/TiO_2 without and with H_2O_2, respectively.

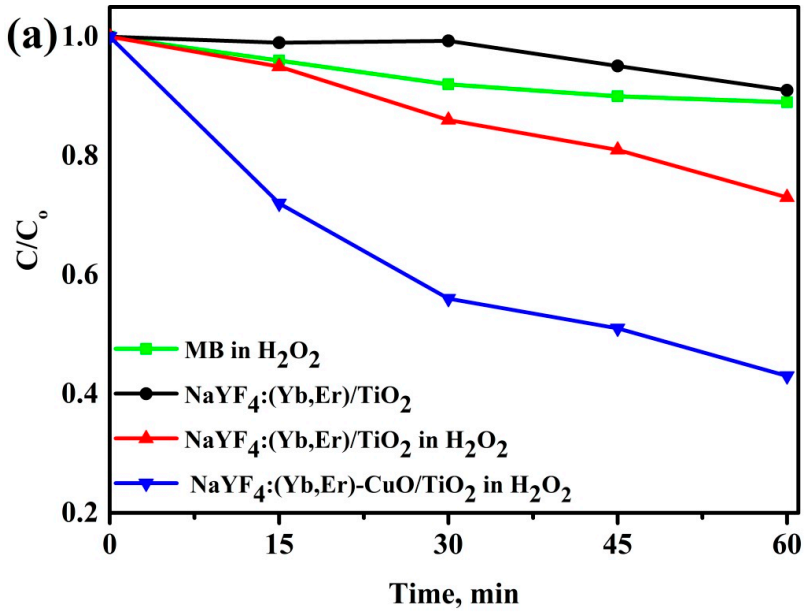

Figure 6. *Cont.*

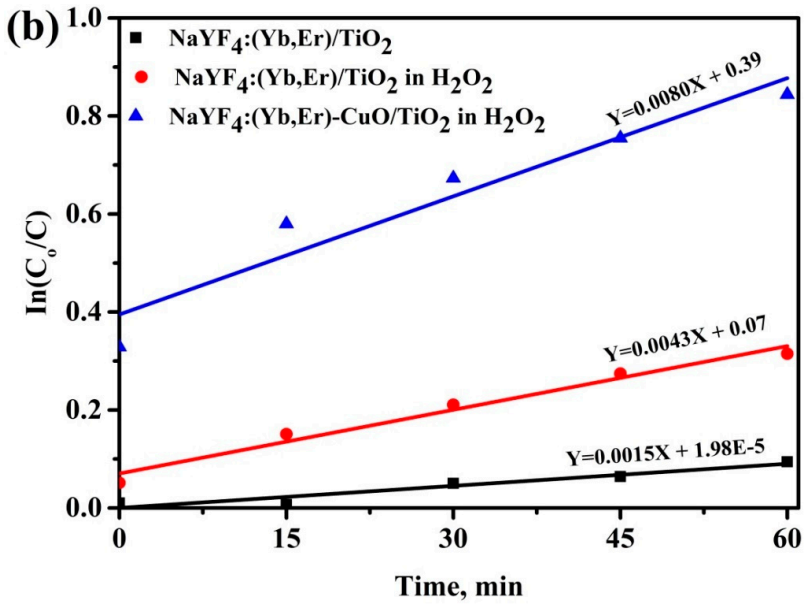

Figure 6. Degradation efficiency of methylene blue (MB) solutions mixed with (**a**) $NaYF_4$:(Yb,Er)-CuO/TiO_2 composites and (**b**) rate kinetics for the samples in (**a**).

Figure 7a shows the photo-degradation efficiency of MB solution with and without H_2O_2 for three samples: $NaYF_4$:(Yb,Er)/TiO_2, $NaYF_4$:(Yb,Er)-CuO and $NaYF_4$:(Yb,Er)-CuO/TiO_2 under visible light. Clearly, the $NaYF_4$:(Yb,Er)-CuO/TiO_2 composite in H_2O_2 has the most efficient photo-activity by decomposing the MB solution more than 99.5% after exposure to visible light. This photocatalytic activity has higher efficiency as compared to only TiO_2-coated phosphor in our previous work [16] and other research [33,43]. The coupling of CuO nanoparticles with $NaYF_4$:(Yb, Er)/TiO_2 caused the formation of visible light-active nanocomposites. Thus, the $NaYF_4$:(Yb, Er)-CuO/TiO_2 nanocomposites and H_2O_2 oxidant molecules enhanced photo-activation and separation of electron-hole pairs for improved photocatalytic activity. Figure 7b shows the recyclability of the $NaYF_4$:(Yb,Er)-CuO/TiO_2 composite under visible light for three cycles. After the first run, the photocatalytic degradation efficiency of the MB solution decreased from almost 100% to 80% and almost 60% in the second and third cycle, respectively. The noticeable difference in photocatalyst efficiency is due to several factors relating to surface-adsorption characteristics, such as Cu leaching [44] and the possible loss of TiO_2 nanoparticles [43]. Specifically, the centrifugal process and several washing steps during material preparation may result in a loss of TiO_2 nanoparticles.

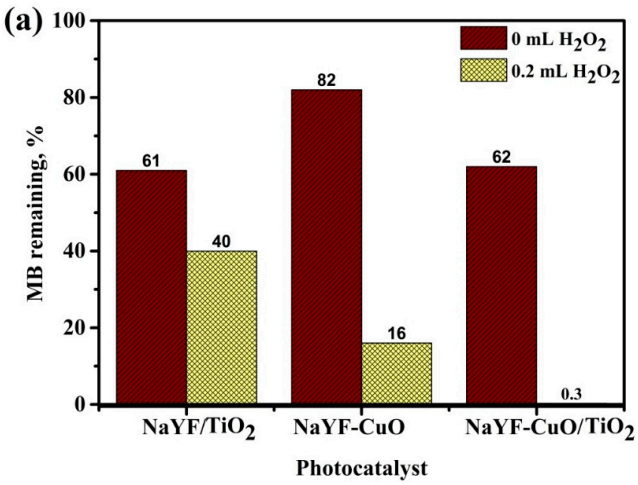

Figure 7. *Cont.*

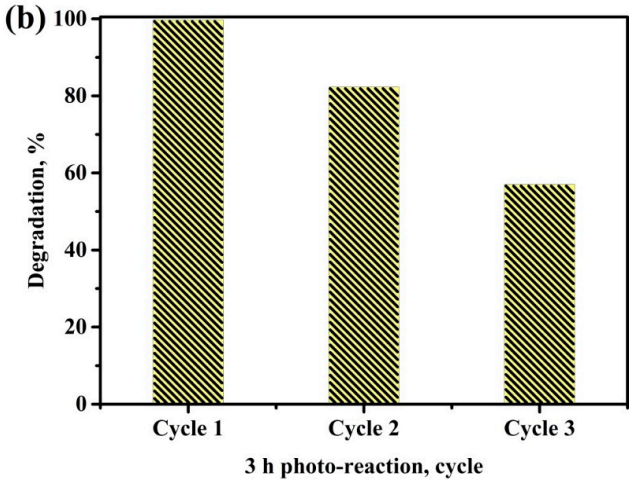

Figure 7. Photo-degradation of the MB solution (**a**) with and without H_2O_2 for $NaYF_4$:(Yb,Er)/TiO_2, $NaYF_4$:(Yb,Er)-CuO and $NaYF_4$:(Yb,Er)-CuO/TiO_2 under visible light for 3 h (NaYF represents $NaYF_4$:(Yb,Er)) and (**b**) the recyclability of the $NaYF_4$:(Yb,Er)-CuO/TiO_2 composite.

The overall photocatalytic activity can be influenced by the chemical composition, specific surface area, optical property of the photocatalyst and the presence of H_2O_2 oxidant molecules [39]. Firstly, the change in compositional crystallinity by coupling $NaYF_4$:(Yb,Er)/TiO_2 with CuO evidently improved the photocatalytic activity. Moreover, the co-existence of CuO, α-$NaYF_4$ and β-$NaYF_4$ phases as confirmed by XRD further increases the TiO_2 absorption edge towards visible light. Secondly, it is well known that the high specific surface area is related to the enhancement of photocatalytic activity. Nevertheless, the case is unique in the $NaYF_4$:(Yb,Er)/TiO_2 and $NaYF_4$:(Yb,Er)-CuO/TiO_2 photocatalyst composites. Thus, $NaYF_4$:(Yb,Er)/TiO_2 showed higher specific area (15.9 m^2/g), but exhibited lower photocatalytic activity than the $NaYF_4$:(Yb,Er)-CuO/TiO_2 (12.4 m^2/g) [45]. The explanation for this discrepancy is regardless of the specific surface area; the dominating property is the existence of a visible light-active CuO compound. Therefore, with CuO nanoparticle coupling (as the third compound in the $NaYF_4$:(Yb,Er)-CuO/TiO_2 composite) visible light absorption by composites is improved and these composites have more efficient charge transfer properties than only TiO_2 coated phosphor [33]. Thirdly, the photoactivity is low without H_2O_2 oxidant molecules in the photo-reaction mixture of TiO_2 coated composites ($NaYF_4$:(Yb, Er)/TiO_2 and $NaYF_4$:(Yb,Er)-CuO/TiO_2) and $NaYF_4$:(Yb,Er)-CuO as exhibited in Figure 7a. Although photo-degradation up to 40% is observed in the TiO_2-coated composites, the $NaYF_4$:(Yb,Er)-CuO degraded only 20% of MB solution. This is due to the higher oxidizing ability of TiO_2 as compared to CuO [46]. In contrast, the photocatalyst mixture with H_2O_2 oxidant molecules showed an improvement in photocatalytic activity of the $NaYF_4$:(Yb,Er)/TiO_2, $NaYF_4$:(Yb,Er)-CuO and $NaYF_4$:(Yb,Er)-CuO/TiO_2. Thus, the H_2O_2 oxidant was photo-degraded to produce hydroxyl and super oxide ions which might degrade the MB-dye solution. The superior oxidizing power of H_2O_2 molecules has been utilized in several research studies to enhance the photocatalytic activity of pure CuO and its composite materials [47]. Finally, the major advantage of coupling CuO and TiO_2 nanoparticles with phosphor is the inevitable alteration of the $NaYF_4$:(Yb,Er)-CuO/TiO_2 composites band structure, as observed in both visible light absorption and band gap estimations in Figure 4. The $NaYF_4$:(Yb,Er) can also facilitate the electron-hole charge separation process which enhances photocatalytic efficiencies [17]. Additionally, the phosphor crystalline surface not only supports the nanoparticles, but it also facilitates energy transfer within the composite system as described in Figure 5c. Accordingly, the composites can also be utilized efficiently in solar harvesting systems.

3. Materials and Methods

$NaYF_4$:(Yb, Er) phosphor was synthesized by solution combustion as described in our previous work [16]. A yttrium rare earth nitrate solution consisting of Y_2O_3 (99.99%, Daejung Chemicals & Metals Co., Ltd., Siheung-si, Gyeonggi-do, Korea), Yb_2O_3 (99.9%, Wako Pure Chemical Industries Ltd., Osaka, Japan) and Er_2O_3 (99.9%, Sigma Aldrich, Shanghai, China) with 0.77:0.2:0.03 molar ratios, respectively, was prepared under magnetic stirring in nitric acid. The fuel mixture of Na_2SiF_6 (98.0%, Duksan Pure Chemical Co., Ltd., Ansansi, Kyunggido, Korea), $CO(NH_2)_2$ (99.0%, Samchun Pure Chemical Co., Ltd., Pyeongtaek, Gyeonggi-do, Korea) and NH_4HF_2 (95.0%, Duksan Pure Chemical Co., Ltd., Ansansi, Kyunggido, Korea) was added to the rare earth yttrium nitrate solution and placed in a muffle furnace (SK1700-B30, Thermotechno Co., Siheung-si, Gyeonggi-do, Korea) for combustion at 650 °C for 5 min. Simultaneously, 4.5 g of $Cu(NO_3)_2{\cdot}3H_2O$ (99.5%, Junsei Chemical Co., Ltd., Tokyo, Japan) was dissolved in 100 mL of distilled water, following by a 1 mL acetic acid (99.0%, Duksan Pure Chemical Co., Ltd., Ansansi, Kyunggido, Korea) addition and magnetic stirring for 1 h at 100 °C. Then, 8 M NaOH (Duksan Pure Chemical Co., Ltd., Ansansi, Kyunggido, Korea) was added to obtain a black CuO precipitate followed by filtering, washing with distilled water and annealing at 500 °C for 4 h. Then, $NaYF_4$:(Yb, Er)-CuO composites at 80:20 wt.% ratio were mixed with ball milling and annealed at 450 °C. Finally, $NaYF_4$:(Yb, Er)-CuO composites were coated with 0.4 M TiO_2-sol prepared from titanium (IV) n-butoxide (99.0%, Acros Organics, Morris, NJ, USA), 50 mL of ethyl alcohol (99.9%, Duksan Pure Chemical Co., Ltd., Ansansi, Kyunggido, Korea) and 10 mL of distilled water at 50 °C. The TiO_2-coated composites were dried at 100 °C in an electric oven for 12 h and calcined at 450 °C for 2 h.

The synthesized samples of $NaYF_4$:(Yb,Er)-CuO/TiO_2 were characterized for crystallinity by a X-ray diffraction (XRD, D8 Discover, Bruker AXS GmbH, Karlsruhe, Germany) with Cu Kα radiation. The morphology of the powder samples was analyzed by scanning electron microscope (SEM, Hitachi S-4300, Hitachi Ltd., Tokyo, Japan). The chemical composition of the composite sample was examined by energy dispersive spectroscopy (EDS, JEOL, JP/JSM-6330F, Kyoto, Japan). The particle size analysis of the $NaYF_4$:(Yb,Er)-CuO/TiO_2 composite was obtained by a particle size analyzer (Microtrac, S-3500, Largo, FL, USA). The specific surface area of the photocatalyst was determined by the Brunauer-Emmett-Teller (BET) method on an N_2 based chemisorption-physisorption micropore analyzer (3flex Micromeritics, Norcross, GA, USA). The photoluminescence (PL) spectra were obtained by a fluorescence spectrophotometer (F-4200, Hitachi, Tokyo, Japan) with an excitation slit of 5 nm and 10 nm emission slit. UV-vis diffuse reflectance spectra were observed using an UV-vis spectrophotometer (UV-1601, Shimadzu, Kyoto, Japan).

The photocatalytic activity was examined by monitoring the UV-vis absorbance of 2 ppm methylene blue (MB, 95.0%, Duksan Pure Chemical Co., Ltd., Ansansi, Kyunggido, Korea) solution under 200 W (clear, Ilkwang Co., Ltd., Dalseogu, Daegu, Korea) visible light irradiation with a 410 nm filter on top of beaker (UV L41 (W) 82 mm, Kenko Zeta, Tokina Co., Ltd., Tokyo, Japan). Prior to irradiation, photocatalyst powders weighing 100 mg were dispersed in a 100 mL beaker of MB solution. Then, the photo-reaction mixture was magnetically stirred for 30 min in darkness to achieve adsorption-desorption equilibria. For comparisons, photo-degradation efficiency was examined with 0.2 mL and without H_2O_2 (28.0%, Duksan Pure Chemical Co., Ltd., Ansansi, Kyunggido, Korea) oxidant molecules. The degradation rate of MB solution mixed with photocatalyst composites was studied by sampling a small amount of solution photo-degraded at 15 min intervals for 1 h. Then, the photocatalyst-mixed solution was further exposed to visible light for 2 h to achieve a 3 h degradation cycle. After the first 3 h cycle, the photocatalyst-mixed solution was centrifugated and washed with ethanol in water to remove adsorbed dye. Then, the photocatalyst powders were dried in an electric oven for 100 °C for 2 h. The recyclability test was carried out for 2 more cycles with the collected $NaYF_4$:(Yb,Er)-CuO/TiO_2 powders using the described photoactivity measurement. The photo-reaction beaker was placed in an ice-water bath to avoid temperature rise during the experiment. Photocatalyst concentration was maintained at 1 mg/mL of MB solution with 0.2 mL

H_2O_2 oxidant. The photo-degraded MB solution was centrifugated and examined for absorption by an UV-vis-NIR spectrophotometer (UV-3150, Shimadzu, Kyoto, Japan).

4. Conclusions

A visible light photo-active $NaYF_4$:(Yb,Er)-CuO/TiO_2 composite has been synthesized. The increase in annealing temperature enhanced the crystallinity of the $NaYF_4$:(Yb,Er)-CuO/TiO_2 composite. The combination of $NaYF_4$:(Yb,Er), CuO and TiO_2 greatly enhances UV-vis optical properties and photocatalytic degradation efficiency for MB solution under visible light irradiation. The $NaYF_4$:(Yb,Er)-CuO/TiO_2 photocatalyst exhibited some recyclability of up to 60% in the third cycle, which could be beneficial for possible application in photocatalyst systems.

Author Contributions: Supervision, J.-S.K.; writing—original draft, S.M.; writing—review and editing, S.-C.J.

Funding: This research work was supported by a grant (17-CTAP-C133057-01) from the Ministry of Land, Infrastructure, and Transport of the Korean government.

Conflicts of Interest: The authors declare no conflict of interest.

References

1. Henderson, M.A. A surface science perspective on TiO_2 photocatalysis. *Surf. Sci. Rep.* **2011**, *66*, 185–297. [CrossRef]
2. Litter, M.I. Heterogeneous photocatalysis: Transition metal ions in photocatalytic systems. *Appl. Catal. B Environ.* **1999**, *23*, 89–114. [CrossRef]
3. Fujishima, A.; Rao, T.N.; Tryk, D.A. Titanium dioxide photocatalysis. *J. Photochem. Photobiol. C Photochem. Rev.* **2000**, *1*, 1–21. [CrossRef]
4. Yadav, H.M.; Kim, J.S. Solvothermal synthesis of anatase TiO_2-graphene oxide nanocomposites and their photocatalytic performance. *J. Alloys Compd.* **2016**, *688*, 123–129. [CrossRef]
5. Luna, A.L.; Valenzuela, M.A.; Justin, C.C.; Vázquez, P.; Rodriguez, J.L.; Avendaño, J.R.; Alfaro, S.; Tirado, S.; Garduño, A.; Rosa, J.M.D. Photocatalytic degradation of gallic acid over CuO-TiO_2 composites under UV/Vis LEDs irradiation. *Appl. Catal. A Gen.* **2016**, *521*, 140–141. [CrossRef]
6. Gupta, K.; Singh, R.P.; Pandey, A.; Pandey, A. Photocatalytic antibacterial performance of TiO_2 and Ag-doped TiO_2 against *S. Aureus. P. Aeruginosa* and *E. Coli. Beilstein J. Nanotechnol.* **2013**, *4*, 345–351. [CrossRef] [PubMed]
7. Kitano, M.; Matsuoka, M.; Ueshima, M.; Anpo, M. Recent developments in titanium oxide-based photocatalysts. *Appl. Catal. A Gen.* **2007**, *325*, 1–14. [CrossRef]
8. Kubacka, A.; Colón, G.; García, M.F. Cationic (V, Mo, Nb, W) doping of TiO_2-anatase: A real alternative for visible light-driven photocatalysts. *Catal. Today* **2009**, *143*, 286–292. [CrossRef]
9. Dozzi, M.V.; Selli, E. Doping TiO_2 with p-block elements: Effects on photocatalytic activity. *J. Photochem. Photobiol. C Photochem. Rev.* **2013**, *14*, 13–28. [CrossRef]
10. Dahl, M.; Liu, Y.; Yin, Y. Composite Titanium Dioxide Nanomaterials. *Am. Chem. Soc.* **2014**, *114*, 9853–9889. [CrossRef] [PubMed]
11. Araque, D.G.; Peña, P.A.; Ortega, D.R.; Rojas, L.L.; Gómez, R. SnO_2-TiO_2 structures and the effect of CuO, CoO metal oxide on photocatalytic hydrogen production. *J. Chem. Technol. Biotechnol.* **2017**, *92*, 1531–1539. [CrossRef]
12. Lafond, V.; Mutin, P.H.; Vioux, A. Non-hydrolytic sol-gel routes based on alkyl halide elimination: Toward better mixed oxide catalysts and new supports application to the preparation of a SiO_2-TiO_2 epoxidation catalyst. *J. Mol. Catal. A Chem.* **2002**, *182–183*, 81–88. [CrossRef]
13. Pan, J.H.; Sun, D.D.; Lee, W.I. Preparation of periodically organized mesoporous bicomponent TiO_2 and SnO_2-based thin films by controlling the hydrolytic kinetics of inorganic precursors during EISA process. *Mater. Lett.* **2011**, *65*, 2836–2840. [CrossRef]
14. Kim, J.-S.; Sung, H.-J.; Kim, B.-J. Photocatalytic characteristics for the nanocrystalline TiO_2 on the Ag-doped $CaAl_2O_4$:(Eu,Nd) phosphor. *Appl. Surf. Sci.* **2015**, *334*, 151–156. [CrossRef]
15. Wang, S.; Wang, L. Lanthanide-doped nanomaterials for luminescence detection and imaging. *TrAC Trends Anal. Chem.* **2014**, *62*, 123–134. [CrossRef]

16. Mavengere, S.; Yadav, H.M.; Kim, J.-S. Photocatalytic properties of nanocrystalline TiO_2 coupled with up-conversion phosphors. *J. Ceram. Sci. Tech.* **2017**, *8*, 67–72.
17. Xu, D.-X.; Lian, Z.-W.; Fu, M.-L.; Yuan, B.; Shi, J.-W.; Cui, H.-J. Advanced near-infrared-driven photocatalyst: Fabrication, characterization, and photocatalytic performance of β-$NaYF_4$:Yb^{3+},Tm^{3+}@TiO_2 core@shell microcrystals. *Appl. Catal. B Environ.* **2013**, *142*, 377–386. [CrossRef]
18. Hsu, C.H.; Lu, C.H. Microwave-hydrothermally synthesized $(Sr_{1-x-y}Ce_xTb_y)Si_2O_2$- $Si_2O_{2-\delta}$ $N_{2+\mu}$ phosphors: Efficient energy transfer, structural refinement and photoluminescence properties. *J. Mater. Chem.* **2011**, *21*, 2932–2939. [CrossRef]
19. Liu, Y.; Xia, Y.; Jiang, Y.; Zhang, M.; Sun, W.; Zhao, X.-Z. Coupling effects of Au-decorated core-shell β-$NaYF_4$:Er/Yb@SiO_2 microprisms in dye-sensitized solar cells: Plasmon resonance versus upconversion. *Electrochim. Acta.* **2015**, *180*, 394–400. [CrossRef]
20. Schietinger, S.; Menezes, L.D.S.; Lauritzen, B.; Benson, O. Observation of size dependence in multicolor upconversion in single Yb^{3+}, Er^{3+} Codoped $NaYF_4$ nanocrystals. *Nano Lett.* **2009**, *9*, 2477–2481. [CrossRef] [PubMed]
21. Bednarkiewicz, A.; Wawrzynczyk, D.; Nyk, M.; Samoć, M. Tuning red-green-white up-conversion color in nano $NaYF_4$:Er/Yb phosphor. *J. Rare Earths* **2011**, *29*, 1152–1156. [CrossRef]
22. Wu, X.; Yin, S.; Dong, Q.; Liu, B.; Wang, Y.; Sekino, T.; Lee, S.W.; Sato, T. UV, visible and near-infrared lights induced NOx destruction activity of (Yb,Er)-$NaYF_4$/C-TiO_2 composite. *Sci. Rep.* **2013**, *3*, 1–8. [CrossRef] [PubMed]
23. Wang, D.; Xiao, L.; Luo, Q.; Li, X.; An, J.; Duan, Y. Highly efficient visible light TiO_2 photocatalyst prepared by sol-gel method at temperatures lower than 300 °C. *J. Hazard. Mater.* **2011**, *192*, 150–159. [CrossRef] [PubMed]
24. Tang, Y.; Di, W.; Zhai, X.; Yang, R.; Qin, W. NIR-responsive photocatalytic activity and mechanism of $NaYF_4$:Yb,Tm@TiO_2 core-shell nanoparticles. *ACS Catal.* **2013**, *3*, 405–412. [CrossRef]
25. Tabaei, H.S.M.; Kazemeini, M.; Fattahi, M. Preparation and characterization of visible light sensitive nano titanium dioxide photocatalyst. *Sci. Iran.* **2012**, *19*, 1626–1631. [CrossRef]
26. Ma, L.; Jia, I.; Guo, X.; Xiang, L. Current status and perspective of rare earth catalytic materials and catalysis. *Chin. J. Catal.* **2014**, *35*, 108–119. [CrossRef]
27. Li, X.; Zhu, Z.; Li, F.; Huang, Y.; Hu, X.; Huang, H.; Peng, R.; Zhai, X.; Fu, Z.; Lu, Y. Multifunctional single-phase photocatalysts: Extended near infrared photoactivity and reliable magnetic recyclability. *Sci. Rep.* **2015**, *5*, 15511. [CrossRef] [PubMed]
28. Wang, W.; Huang, W.; Ni, Y.; Lu, C.; Xu, Z. Different upconversion properties of β-$NaYF_4$:Yb^{3+}, Tm^{3+}/Er^{3+} in Affecting the near-infrared-driven photocatalytic activity of high-reactive TiO_2. *ACS Appl. Mater. Interfaces.* **2014**, *6*, 340–348. [CrossRef] [PubMed]
29. Yadav, H.M.; Kolekar, T.V.; Pawar, S.H.; Kim, J.-S. Enhanced photocatalytic inactivation of bacteria on Fe-containing TiO_2 nanoparticles under fluorescent light. *J. Mater. Sci. Mater. Med.* **2016**, *27*, 57. [CrossRef] [PubMed]
30. Reszczyńska, J.; Grzyb, T.; Sobczak, J.W.; Lisowski, W.; Gazda, M.; Ohtani, B.; Zaleska, A. Lanthanide co-doped TiO_2: The effect of metal type and amount on surface properties and photocatalytic activity. *Appl. Surf. Sci.* **2014**, *307*, 333–345. [CrossRef]
31. Deboer, M.A.; Lammertsma, K. Scarcity of rare earth elements. *ChemSusChem* **2013**, *6*, 2045–2055. [CrossRef] [PubMed]
32. Wang, F.; Han, Y.; Lim, C.S.; Lu, Y.; Wang, J.; Xu, J.; Chen, H.; Zhang, C.; Hong, M.; Liu, X. Simultaneous phase and size control of upconversion nanocrystals through lanthanide doping. *Nature* **2010**, *463*, 1061–1065. [CrossRef] [PubMed]
33. Guo, X.; Di, W.; Chen, C.; Liu, C.; Wang, X.; Qin, W. Enhanced near-infrared photocatalysis of $NaYF_4$:Yb, Tm/CdS/TiO_2 composites. *Dalt. Trans.* **2014**, *43*, 1048–1054. [CrossRef] [PubMed]
34. Luoshan, M.; Bai, L.; Bu, C.; Liu, X.; Zhu, Y.; Guo, K.; Jiang, R.; Li, M.; Zhao, X. Surface plasmon resonance enhanced multi-shell-modified upconversion $NaYF_4$:Yb^{3+}, Er^{3+}@SiO_2@Au@TiO_2 crystallites for dye-sensitized solar cells. *J. Power Sources* **2016**, *307*, 468–473. [CrossRef]
35. Zhang, H.; Millington, K.R.; Wang, X. The photostability of wool doped with photocatalytic titanium dioxide nanoparticles. *Polym. Degrad. Stab.* **2009**, *94*, 278–283. [CrossRef]

36. Luo, L.; Li, Y.; Hou, J.; Yang, Y. Visible photocatalysis and photostability of Ag_3PO_4 photocatalyst. *Appl. Surf. Sci.* **2014**, *319*, 332–338. [CrossRef]
37. Deng, X.; Wang, C.; Shao, M.; Xu, X.; Huang, J. Low-temperature solution synthesis of CuO/Cu_2O nanostructures for enhanced photocatalytic activity with added H_2O_2: Synergistic effect and mechanism insight. *RSC Adv.* **2017**, *7*, 4329–4338. [CrossRef]
38. Wang, C.; Zhang, X.; Liu, Y. Promotion of multi-electron transfer for enhanced photocatalysis: A review focused on oxygen reduction reaction. *Appl. Surf. Sci.* **2015**, *358*, 28–45. [CrossRef]
39. Sahel, K.; Elsellami, L.; Mirali, I.; Dappozze, F.; Bouhent, M.; Guillard, C. Hydrogen peroxide and photocatalysis. *Appl. Catal. B Environ.* **2016**, *188*, 106–112. [CrossRef]
40. Ratnasamy, P.; Srinivas, D.; Knözinger, H. Active sites and reactive intermediates in titanium silicate molecular sieves. *Adv. Catal.* **2004**, *48*, 1–169.
41. Dubale, A.A.; Pan, C.; Tamirat, A.G.; Chen, H.-M.; Su, W.-N.; Chen, C.-H.; Rick, J.; Ayele, D.W.; Aragaw, B.A.; Lee, J.-F.; et al. Heterostructured Cu_2O/CuO decorated with nickel as a highly efficient photocathode for photoelectrochemical water reduction. *J. Mater. Chem. A* **2015**, *3*, 12482–12499. [CrossRef]
42. Singh, V.; Haritha, P.; Venkatramu, V.; Kim, S.H. Efficient visible upconversion luminescence in Er^{3+} and Er^{3+}/Yb^{3+} co-doped Y_2O_3 phosphors obtained by solution combustion reaction. *Spectrochim. Acta A Mol. Biomol. Spectrosc.* **2014**, *126*, 306–311. [CrossRef] [PubMed]
43. Wu, T.; Long, J.; Fan, Z.; Du, M.; Xiong, S.; Zhao, D.; Ji, F.; He, Q.; Zeng, Y.; Xu, X. Synthesis and photocatalytic activity of hexagonal phase $NaYF_4$:Ho^{3+}@TiO_2 core–shell microcrystals. *CrystEngComm* **2016**, *18*, 6471–6482. [CrossRef]
44. Gombac, V.; Sordelli, L.; Montini, T.; Delgado, J.J.; Adamski, A.; Adami, G.; Cargnello, M.; Bernal, S.; Fornasiero, P. CuO_x-TiO_2 Photocatalysts for H_2 production from ethanol and glycerol solutions. *J. Phys. Chem. A* **2010**, *114*, 3916–3925. [CrossRef] [PubMed]
45. Liu, Y.; Ji, G.; Dastageer, M.A.; Zhu, L.; Wang, J.; Zhang, B.; Chang, X.; Gondal, M.A. Highly-active direct Z-scheme Si/TiO_2 photocatalyst for boosted CO_2 reduction into value-added methanol. *RSC Adv.* **2014**, *4*, 56961–56969. [CrossRef]
46. Paschoalino, F.C.S.; Paschoalino, M.P.; Jordão, E.; Jardim, W.F. Evaluation of TiO_2, ZnO, CuO and Ga_2O_3 on the photocatalytic degradation of phenol using an annular-flow photocatalytic reactor. *Open J. Phys. Chem.* **2012**, *2*, 135–140. [CrossRef]
47. Deng, X.; Zhang, Q.; Zhao, Q.; Ma, L.; Ding, M.; Xu, X. Effects of architectures and H_2O_2 additions on the photocatalytic performance of hierarchical Cu_2O nanostructures. *Nanoscale Res. Lett.* **2015**, *10*, 2–10. [CrossRef] [PubMed]